

Minimizing scatter-losses during pre-heat for magneto-inertial fusion targets

Matthias Geisse,^{a)} Adam J. Harvey-Thompson, Thomas J. Awe, David E. Bliss, Michael E. Glinsky, Matthew R. Gomez, Eric Harding, Stephanie B. Hansen, Christopher Jennings, Mark W. Kimmel, Patrick Knapp, Sean M. Lewis, Kyle Peterson, Marius Schollmeier, Jens Schwarz, Jonathon E. Shores, Stephen A. Slutz, Daniel B. Sinars, Ian C. Smith, C. Shane Speas, Roger A. Vesey, Matthew R. Weis, and John L. Porter
 Sandia National Laboratories, Z-Backlighter Facility, Albuquerque, New Mexico 87185, USA

(Received 1 September 2017; accepted 2 February 2018; published online 21 February 2018)

The size, temporal and spatial shape, and energy content of a laser pulse for the pre-heat phase of magneto-inertial fusion affect the ability to penetrate the window of the laser-entrance-hole and to heat the fuel behind it. High laser intensities and dense targets are subject to laser-plasma instabilities (LPI), which can lead to an effective loss of pre-heat energy or to pronounced heating of areas that should stay unexposed. While this problem has been the subject of many studies over the last decades, the investigated parameters were typically geared towards traditional laser driven Inertial Confinement Fusion (ICF) with densities either at 10% and above or at 1% and below the laser's critical density, electron temperatures of 3–5 keV, and laser powers near (or in excess of) 1×10^{15} W/cm². In contrast, Magnetized Liner Inertial Fusion (MagLIF) [Slutz *et al.*, Phys. Plasmas **17**, 056303 (2010) and Slutz and Vesey, Phys. Rev. Lett. **108**, 025003 (2012)] currently operates at 5% of the laser's critical density using much thicker windows (1.5–3.5 μ m) than the sub-micron thick windows of traditional ICF hohlraum targets. This article describes the Pecos target area at Sandia National Laboratories using the Z-Beamlet Laser Facility [Rambo *et al.*, Appl. Opt. **44**(12), 2421 (2005)] as a platform to study laser induced pre-heat for magneto-inertial fusion targets, and the related progress for Sandia's MagLIF program. Forward and backward scattered light were measured and minimized at larger spatial scales with lower densities, temperatures, and powers compared to LPI studies available in literature. *Published by AIP Publishing.* <https://doi.org/10.1063/1.5003038>

I. INTRODUCTION

Any magneto-inertial fusion (MIF) concept requires magnetization of the fuel by pre-heating it when already subjected to an initial magnetic field. In Sandia's Magnetized Liner Inertial Fusion (MagLIF) program,^{1,2} the deuterium fuel, which has been exposed to a slowly pulsed magnetic field,⁴ is heated by 526.6 nm laser light from Z-Beamlet³ as sketched in Fig. 1 and is subsequently imploded by a massive pulsed power discharge delivered by Sandia's Z-Facility.⁵ The initial magnetic field is enhanced during the implosion and reduces losses from heat conduction.

First integrated experiments at Sandia have proven fusion-relevant conditions and thermonuclear yields, but the data did not reach the values of initial simulations. It was then assumed that the laser pre-heat for these experiments may have been significantly less than expected⁶ though no experimental data was available to confirm this hypothesis. Simulations suggest that for low preheat energies, MagLIF fusion yields are a strong function of the preheat energy coupled into the fuel. Increasing the preheat energy coupled and ensuring energy is coupled with shot-to-shot reproducibility is therefore very important to optimizing MagLIF performance, while constraining the amount of preheat energy coupled is required to understand the performance.

At the time of preheat, the MagLIF target is a 7.5–10 mm long liner, inner-diameter 4.65 mm, filled with 0.68 mg/cm³

of gaseous D₂ fuel. To contain the D₂ fuel while allowing access to the heating laser, the MagLIF target employs a thin (1.77–3.5 μ m) polyimide window at the laser-entrance-hole (LEH). Before laser light can be effectively transmitted through the LEH window, its density must be reduced to below the critical density. To do this, the laser pulse is typically split into a prepulse followed by a main pulse. The main pulse heats the window, and a delay between the prepulse and main pulse allows the material to expand and reduce its opacity before the main pulse arrives. Window disassembly needs to balance two competing objectives: maximizing the main pulse transmission through the window and minimizing the kinetic energy imparted to the window which can result in the window material being ejected into the imploding fuel region and contributing to mix. Understanding this process is therefore important to the success of MagLIF.

The preferred way for the laser to interact with the gas is by inverse bremsstrahlung absorption whereby laser energy is absorbed by the electrons in a collisionless scattering process. The absorption cross section is dependent on the plasma electron temperature; the initially cold gas will strongly absorb laser energy until its temperature is raised and its opacity drops. What results is a propagating heat front in the plasma along the path of the laser with typical velocities of several mm/ns.

Other less-desirable processes may also play a role in the laser interaction with the MagLIF plasmas, in particular, laser plasma instabilities (LPI) can occur that can have deleterious effects on target performance. Some processes such as Stimulated Brillouin Scattering (SBS),^{7,8} Stimulated Raman

^{a)}Electronic mail: mgeisse@sandia.gov

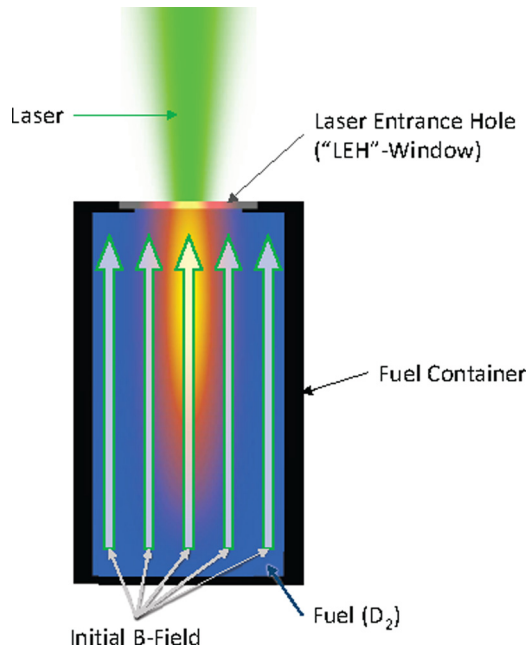


FIG. 1. Sketch of a MagLIF pre-heat scenario.

Scattering (SRS),⁹ and Two-Plasmon Decay (TPD)¹⁰ act to scatter energy out of the target or couple energy into fast electrons which reduces the efficiency of the laser coupling. Filamentation can also occur which acts to enhance intensity modulations and redirect the path of laser energy. This may have the potential to deposit energy at the target walls creating mix and can feed back into other LPI processes by enhancing intensity modulations.

Prior to the start of Sandia's MagLIF program, Z-Beamlet was primarily used as a driver for X-ray backlighting of fusion related experiments on Z,^{11–13} which did not require beam smoothing techniques such as random phase plates (RPP)¹⁴ or the more efficient but equivalent "continuous" or "distributed" phase plates (CPP, DPP),^{15,16} smoothing by spectral dispersion (SSD),¹⁷ polarization smoothing (PS),¹⁸ or induced spatial incoherence (ISI).¹⁹

Initially, it was not expected that LPI would be a dominant problem for the laser interaction with the deuterium fuel because the experiments to date predominantly use pressures around 60 psi of D₂, which lead to electron densities below 5% of the critical density n_c for a wavelength of 527 nm. Laser heating of LPI affected plasmas has been studied before in the context of inertial confinement fusion (ICF), but was typically only considered for densities of 0.1–0.25 n_c .^{20–23} In a MagLIF scenario, such high densities are only present in the short phase of LEH window disassembly. However, if local intensities and beam profile modulations are high enough, they can still cause dramatic LPI effects in lower density plasmas.

Typically, radiation magneto-hydrodynamic (RMHD) models are used to model MagLIF, including the preheat stage. While these models include inverse bremsstrahlung absorption, they do not typically include LPI physics which is complex to model accurately. Generally, it is thought that minimizing LPI during MagLIF preheat will be beneficial in reducing mix, reducing uncertainty about energy deposited,

increasing reproducibility, and will allow the energy deposition to be modelled more accurately. Details of LPI processes and how they relate to MagLIF targets are summarized further in Sec. II.

This paper describes the setup and first results from the Pecos target area, an experimental platform dedicated to investigating MagLIF preheat at Sandia National Laboratories. Two experimental campaigns are described: The first investigates laser energy transmission through LEH foils and factors that affect this, and the second investigates laser energy absorption into MagLIF-relevant gas cells. Foil transmission measurements show that a single foil can transmit almost 100% of the laser energy for sufficiently strong pre-pulses. With decreasing prepulse energy, more and more light is scattered into higher angles and eventually absorbed or backscattered by the generated plasma. Gas cell experiments show that Brillouin backscatter can amount to hundreds of Joules if the laser intensity is chosen too high. By using a distributed phase plate and extended pulse lengths, SBS could be reduced by up to three orders of magnitude. Along with reduced SBS, deeper and narrower energy deposition was observed for the improved laser configuration, which brought experimental observations closer to simulated results.

We will describe relevant mechanisms and threshold figures for laser plasma instabilities in Section II, followed by LEH and gas cell experimental descriptions and results.

II. LASER-PLASMA INSTABILITIES

Laser-plasma instabilities occur when intense laser light changes the property of the medium in which it propagates such that the medium influences the light in a positive feedback pattern. A classical example is filamentation, which occurs when local intensity maxima lead to temperature modulations, which in turn affect the refractive index and cause the light to focus/heat progressively. Plasma modulations are forming the equivalent of little lens arrays with increasing strength. Understanding that hot plasma regions lower the electron density by expelling some of the electrons into cooler regions, filamentation becomes obvious following the dependence of the refractive index N on the electron density n_e ²⁴

$$N^2 \propto \left(1 - \frac{n_e}{n_c}\right). \quad (1)$$

More complex LPI processes include multi-wave mixing. Here, the incoming light wave interacts with ion-acoustic waves or electron-plasma waves, which in turn have been initiated by the coupling of laser light to the plasma. The processes have been described in detail in the literature (see references in Sec. I), and even practical synopses and typical thresholds are published to serve as guidelines for experimenters.²⁵ Each LPI effect grows exponentially with density and laser intensity, and the magnitude of the effect is not governed by the absolute electron density but by the ratio of the electron density n_e to the laser's critical density n_c .

Stimulated Brillouin scattering happens when laser light is coupled to an ion-acoustic wave. The high mass of the ion prohibits efficient energy coupling into the medium,

but light can still be scattered sideways or backwards with high efficiency, albeit with a wavelength that is nearly identical to the wavelength $\lambda_0 = 2\pi c/\omega_0$ of the incident laser. Accordingly, energy transfer into the plasma is much more efficient for stimulated Raman scattering, which couples to electron-plasma waves. The scattered wave of frequency ω_{sc} will be strongly red-shifted for efficient energy transfer, with the extreme being $\omega_{sc} = \omega_0/2$ for direct backscatter in a quarter-critical plasma. Matching conditions prevent SRS from happening at densities above $0.25 n_c$. Right at the quarter-critical density, a laser photon can decay into two electron plasma waves, which is called two-plasmon-decay and presents a very efficient plasma heating process. Apart from a short period during the early destruction of the LEH window, TPD is not a concern for this work since the plasma densities in MagLIF are generally below $0.25 n_c$ to this date.

Table I summarizes relevant LPI processes and their critical parameters with specific thresholds for typical plasma conditions in MagLIF related experiments. The formulas mentioned in the table are meant to be used with parameters in the same units as given in the table and caption. The real threshold value for TPD could be higher because the decompressing LEH window might only provide a fraction of the assumed length near quarter-critical density since the electron density profile will exhibit a steep gradient. A similar caveat applies to SRS and SBS because the temperature in the gas could be higher during the heating process, and the interaction length varies over time. Even though the laser typically penetrates 8–10 mm into the plasma, only a very small fraction of the energy is reaching the end of the range, and the laser intensity at this depth will have significantly decayed due to absorption during the propagation through the plasma. It is difficult to estimate what an appropriately assumed plasma length might be to estimate LPI thresholds based on the maximum propagation depth unless detailed numerical simulations with LPI-capable codes such as pF3D²⁶ are carried out. However, thresholds for the early propagation stage after about 1 mm of plasma length and for 5 mm, about half of the final propagation length, may serve as guidelines.

Many LPI studies have been conducted over the last few decades involving film covered gas containers or gas-bag experiments. Most of these experiments have been motivated

by laser driven Inertial Confinement Fusion (ICF) research. As a result, the majority of the published studies were carried out at different parameters compared to the conditions found in MagLIF. Figure 2 shows a comparison between the parameter space for this work and a variety of well-cited publications in the field. While some experiments were done at the same laser wavelength and density, the vast majority were performed at shorter wavelength and at much higher temperatures and laser intensities. Since an extrapolation for LPI behavior over multiple parameters and over an order of magnitude or more can cause significant errors, a dedicated study for the MagLIF regime was deemed prudent and motivated this work.

III. EXPERIMENTAL METHODS

Two types of experiments have been performed to study and optimize the laser heating process. They did not use a magnetic field and were conducted in the Pecos target chamber of Sandia's Z-Backlighter facility. Caused by the geometry of the laser's beam transport, the orientation of the gas cell is not upright as in an integrated MagLIF experiment, but horizontal such that Z-Beamlet enters from the northern port of the Pecos target chamber towards the south. The first series investigated the transmission through stand-alone foils that are similar or identical to LEH windows in integrated experiments. The energy loss measured in those foils presents a lower limit compared to experiments with a gas cell since the gas pressure will impede the expansion of the foil, thus enhancing the absorption of laser light in the denser material. Experiments for LEH absorption were using a full-beam calorimeter behind the foil to directly measure transmitted energy. Since large angle scattering can occur which causes some energy to miss the calorimeter, a calibrated scatter plate was placed around the calorimeter, assessing beam spread and completing the transmission measurement. Figure 3 shows a sketch of the setup. A second scatter plate was placed at the laser entrance side of the target chamber framing the incident laser envelope. This scatter plate was used to measure stimulated Brillouin backscatter near the laser cone (SBS Near-Beam Imager/NBI). Both scatter plates were imaged in a camera using a mirror, which showed the entire

TABLE I. Synopsis of relevant LPI mechanisms and critical parameters taken from literature²⁵ with numeric threshold values based on approximated current MagLIF parameters: $\lambda = 0.527 \mu\text{m}$, $n_e = 2.17 \times 10^{20} \text{ cm}^{-3}$, and $F \# = 10$. The formula for SRS is generalized in the table but given for direct backscatter ($n_e = 0.25 n_c$) in the cited reference.

	SBS	SRS	TPD	Filamentation
Coupling agent	Ion acoustic wave	Electron plasma wave	Electron plasma wave	Intensity hot spots
Most affected area	Fuel	Fuel	LEH window	Fuel
Density regime	$\leq n_c$	$\leq n_c/4$	$\approx n_c/4$	$< n_c$
Plasma length (μm)	5000	5000	100	(Irrelevant)
Plasma Temp. (keV)	0.5	(Irrelevant)	1	0.5
Electron density	5% n_c	5% n_c	25% n_c	5% n_c
Wavelength shift	$\leq 1\%$	Up to 2×	(annihilated)	None
Concerns	Poor coupling, mix	Poor coupling, mix	Mix	Mix, increased SRS/SBS
Threshold for I	$7 \times 10^{15} T_e n_c$ $L_{\text{plasma}} \lambda n_e$	$1 \times 10^{17} n_c$ $L_{\text{plasma}} \lambda n_e$	$5 \times 10^{15} T_e$ $L_{\text{LEH}} \lambda$	$1 \times 10^{14} \frac{T_e n_c}{F^2 \lambda^2 n_e}$
Threshold value (W/cm ²)	2.7×10^{13}	7.6×10^{14}	1.0×10^{14}	3.6×10^{13}

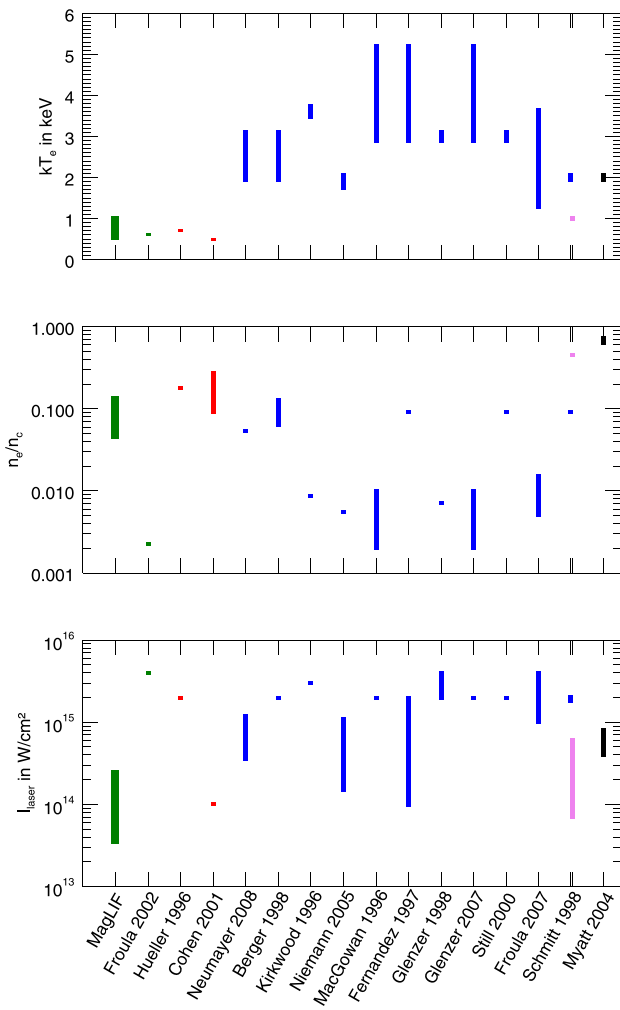


FIG. 2. Comparison of MagLIF parameters (leftmost data entries) to those used in previously published LPI studies. Green data bars refer to studies with a laser wavelength of 527 nm, while red, blue, and violet represent 1054 nm, 351 nm, and 250 nm, respectively. The work of Myatt *et al.* (black data bar) was done with respect to a universal fraction of the critical density for laser light rather than absolute. In addition to the above mentioned publications from Froula,⁸ MacGowan,²⁰ Fernández,²¹ Niemann,²² Glenzer,²³ and Berger,²⁶ we cite work from Hüller,²⁷ Cohen,²⁸ Neumayer,²⁹ Kirkwood,³⁰ Still,³¹ Schmitt,³² and Myatt³³ as well as further work by Froula³⁴ and Glenzer.³⁵ It appears that MagLIF experiments are situated in a niche of experimental conditions.

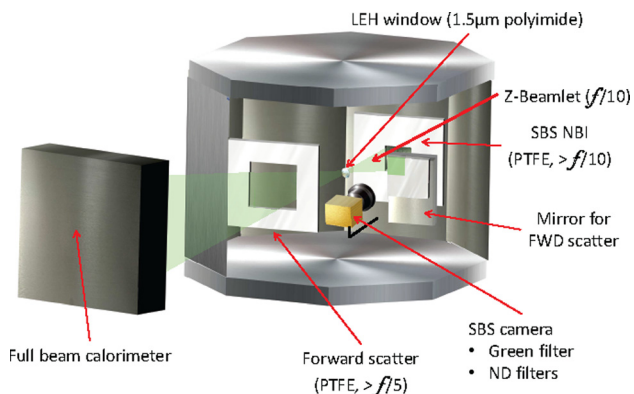


FIG. 3. Sketch of pre-heat experiments in the Pecos target chamber (X-ray diodes and exit window of the chamber not shown). Some wall panels were left out in the cartoon to show the interior of the chamber. The SBS camera is mounted outside the chamber and observes the experiment through a viewport.

transmission scatter plate while still revealing about 50% of the NBI plate. While the missing energy inside the open aperture of the forward-scatter plate is registered by the calorimeter, no measurement for the energy that is scattered back into the laser cone could be performed. Instead, a superposition of two or three 2-dimensional Gaussian distributions was fitted to the NBI profiles in order to get an approximation for the total backscattered energy. The calibration of the scatter plates was done by firing a low energy shot of the Z-Beamlet laser at 526.6 nm onto a solid forward scatter plate (no transmission aperture) with all attenuation filters in place since calibration attempts with lower powered continuous sources revealed a nonlinear behavior of the detection system. The utilized 532 nm interference filter appeared to be a little too narrow for the application, which leads to an increased error for the scattered signal. A representative spectrum taken for a subset of the presented experiments was used to estimate the effect of spectral broadening and shift on the transmission through the interference filter. Figure 4 shows an overlay of the coarsely defined filter specification from the vendor with a super-Gaussian fit and the characteristic SBS spectrum. Based on the 526.6 nm calibration, one over-estimates the amount of SBS by about 15% in this measurement. Spectra were not obtained for every experiment, and both shift and width of the recorded samples varied slightly. This is taken into account by applying asymmetric error bars that allow for more error towards lower values instead of lowering the calculated value by a prescribed amount. The uncertainty in the backscattered energy measurement that results from fitting a distribution to the NBI measurement is more difficult to quantify because the true shape of the backscatter distribution that is lost through the screen's aperture is effectively unknown. In cases of a strong, large-angle backscatter signal, the uncertainty is only near 10% since even exaggerated fit-profiles for the missing parts contribute comparably little to the total signal. In these cases, most of the backscattered solid angle hits the NBI screen. Weak, narrow backscatter signals could be grossly underestimated since the fit relies on remnant edges of an unknown distribution. Thankfully, even a 200%–300%

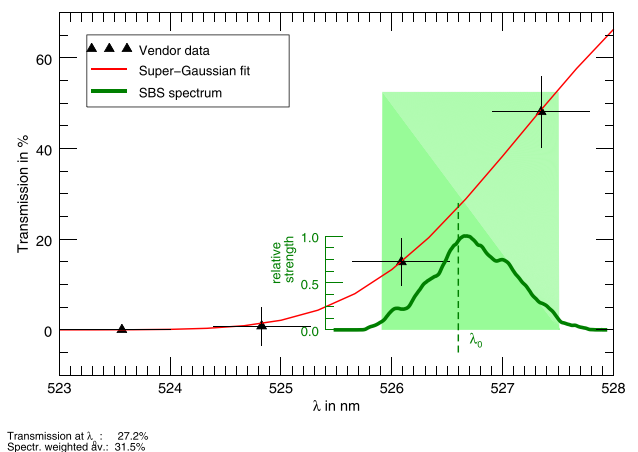


FIG. 4. Plot of vendor provided interference filter data (triangles) with an overlaid super-gaussian fit and a typical SBS spectrum. The calibration at $\lambda_0 = 526.6$ nm leads to an overestimate of the SBS measurement, which predominantly records near better transmitted wavelengths.

error would at most represent a few tens of Joules for weak signals. The presented error bars do not reflect this uncertainty because the magnitude is unknown. Accordingly, the measurements of NBI-SBS backscatter are potentially incomplete and merely intended to document successful LPI reduction. The true values of total backscatter may differ. SRS measurements would be desirable but were not possible at this time due to a lack of calibration options and diagnostic ports. Independent, uncalibrated measurements during MagLIF experiments at the Z facility imply that SRS is predominantly appearing through LEH interaction, which limits the magnitude of SRS backscatter. TPD is neglected here since the fuel is below the required electron density of $0.25 n_c$, as is the LEH plasma soon after being hit by the pre-pulse. As an auxiliary diagnostic, two filtered silicon PIN diodes were placed near the entrance aperture of the laser beam to measure the X-ray response of the target.

The second set of experiments used a plastic cylinder filled with helium gas as a surrogate for the deuterium fuel used in integrated MagLIF experiments because the implementation of a flammable gas permit in the Pecos target area was still pending. Absorption is expected to increase for helium in comparison to deuterium based on its nuclear charge's effect on inverse bremsstrahlung. The fill pressure was decreased by 10% to minimize this effect without decreasing the electron density too much. Table II compares targets for the described experiments to the design used for integrated MagLIF experiments. Since the targets for pre-heat studies did not include a pulsed B-Field and were not imploded by Z, a design could be chosen that gives better observation access to the interior of the cell, including optically transparent diagnostic windows. A probe laser delivering two pulses with orthogonal polarization and variable delay was used to cast a shadow image onto dedicated shadowgraphy CCD cameras. This shadowgraphy technique was used to observe the propagation depth of the laser and the resulting blast wave expansion around the heated plasma. Figure 5 shows the layout of this diagnostic. The imaging lenses had a diameter of 2 in. and separation between the target and the objective lens was 1290 mm. This long F-number effectively functions as a filter that cuts out high spatial frequencies. The recorded image is consequently a combination of a shadow and a bright-field schlieren setup since absorption as well as high-angle scatter and refraction in

TABLE II. Comparison of gas cells in the PECOS target chamber and MagLIF targets.

	Preheat (PECOS)	MagLIF (Z)
Outer diameter (mm)	38	5.4
Internal length (mm)	52	7.5–10
Cell body	Polycarbonate	Beryllium
LEH material	Polyimide	Polyimide
LEH thickness (μm)	1.7	1.7
LEH diameter (mm)	3	3
Fill gas	Helium	Deuterium
Fill pressure (psi)	54	60
Seed B-field (T)	...	10
Diagn. window (mm)	$\varnothing = 25.4$...

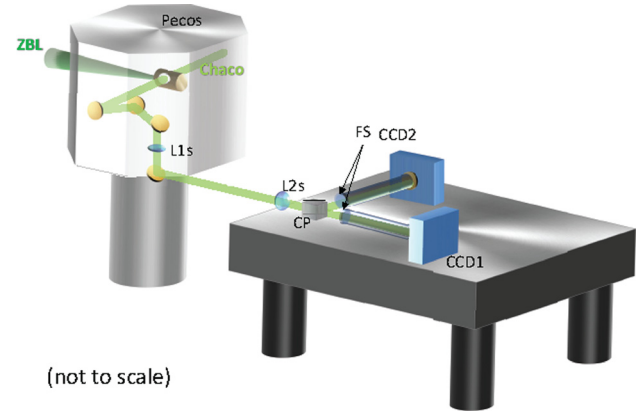


FIG. 5. Cartoon of the shadowgraphy technique. The Chaco probe laser passes through the gas cell perpendicular to the Z-Beamlet laser (ZBL) and serves as a bright backlighter. The target is imaged with a demagnifying two-lens system (L1s, L2s) onto the CCD sensors, using a cubic polarizer (CP) to split the polarizations carrying the two temporally separated frames. Target self-emission and background light are suppressed by filter stacks (FS) and black plastic tubing.

the target can produce dark regions in the image. This concept was chosen over traditional dark-field schlieren imaging in order to accommodate smaller optics that could be protected more easily and provide more flexibility in the optical design. One pixel on the CCD sensor represented $15.1 \mu\text{m}$ in the target plane, and the effective optical resolution was $60\text{--}100 \mu\text{m}$, limited by the aperture of the lenses and alignment uncertainties. Two shadowgraphs were recorded directly after the end of the laser's main pulse and about 20 ns later via two orthogonally polarized probe pulses that were separated in a polarizing beam splitter cube. The first frame provided the laser propagation depth along with a qualitative shape of the heated region, thus giving indications about potential mix and the fidelity of idealized (LPI-free) computer simulations in HYDRA.³⁶ It is the goal of pre-heat studies to achieve conditions that are predictable by simulations, which is an important requirement for the success of further experimental designs. The second frame allowed for some blast wave propagation intended for a more quantitative assessment of the deposited energy, which is not within the scope of this article but will be published separately. The gas cell experiments also used the same X-ray diodes and NBI scatter plate as the LEH experiments but had no transmission measurements apart from interpreting the shadowgraphs. The X-ray diodes recorded the LEH response and as much of the fuel response as could be observed through the LEH. The laser propagation into the gas was always shorter than the gas cell dimensions, which allowed for a 25 mm observation window.

Experiments with gas cells used three different focus geometries. Two experiments were done without any phase plate conditioning while shifting the focus 3.5 mm in front of the LEH window. All other experiments used either a $1100 \mu\text{m}$ DPP or a $750 \mu\text{m}$ DPP. The 1100 and 750 designations originate from the University of Rochester's Laboratory for Laser Energetics. The DPPs were designed to achieve 95% energy containment within a diameter of $750 \mu\text{m}$ or $1100 \mu\text{m}$ with the Omega-EP laser. The actual diameters for Z-Beamlet are different due to different properties of the laser beam and

focusing optics. Figure 6 compares the unconditioned, defocused beam as used for previous integrated MagLIF experiments as well as the focus images of the DPP750 and DPP1100 in the PECOS target chamber. The regions of characteristic intensity are well defined by the FWHM of the phase plates, which contain about 75% of the laser energy (white dashed circles). An equivalent area of the unconditioned beam is harder to define, but a rectangular area that encircles 75% of the laser energy along the highest intensity regions can be found (white dashed rectangle). The size of the 75% containment areas for each focal geometry is noted below the focus images. Even though an average laser intensity is poorly defined for experiments without phase plate, the 75% area of $1.33 \times 10^{-3} \text{ cm}^2$ will be used to determine a representative focus intensity for plots in Sec. V.

IV. SUPPORTING SIMULATIONS

A number of 2D HYDRA simulations were run to support and understand the experimental findings. HYDRA incorporates a vast array of physics, including radiation transport in absence of local thermal equilibrium, MHD with self-generated magnetic fields, anisotropic thermal conduction and laser raytracing. However, a significant limitation of the code, in the context of this work, is the inability to model

LPI losses in a self-consistent way. One exception is filamentation, which HYDRA has some ability to capture. In the context of simulations, phase plates do not only reduce LPI but also facilitate modeling of the experiment. Though we cannot truly predict the evolution of LPI, HYDRA calculations can be post-processed using the NEWLIP code,³⁷ to assess the potential for LPI. NEWLIP performs a linear gain calculation for SBS and SRS along the rays in the HYDRA simulation, using the plasma parameters calculated in the simulation. We show some brief results of these calculations to illustrate their utility but the modeling of these experiments extends beyond the scope of this article and will be a focus of a future publication.

Simulations of the gas cell experiments B16072205 (DPP750, 100 TW/cm^2), B16083014 (DPP1100, 50 TW/cm^2), and B16100604 (DPP1100, 35 TW/cm^2) were performed and post-processed. B16070804 (DPP750, 190 TW/cm^2) produced too much LPI to be a viable calculation. The laser source in the simulations follows the measured power history for each of the shots, and it uses the measured phase plate profile. There is uncertainty in the pointing of the laser as well as the depth of focus, which are assumed perfect in the simulation. The polyimide windows in the simulation are all set to be $1.6 \mu\text{m}$ thick with a 600 nm deflection (an average value determined from metrology).

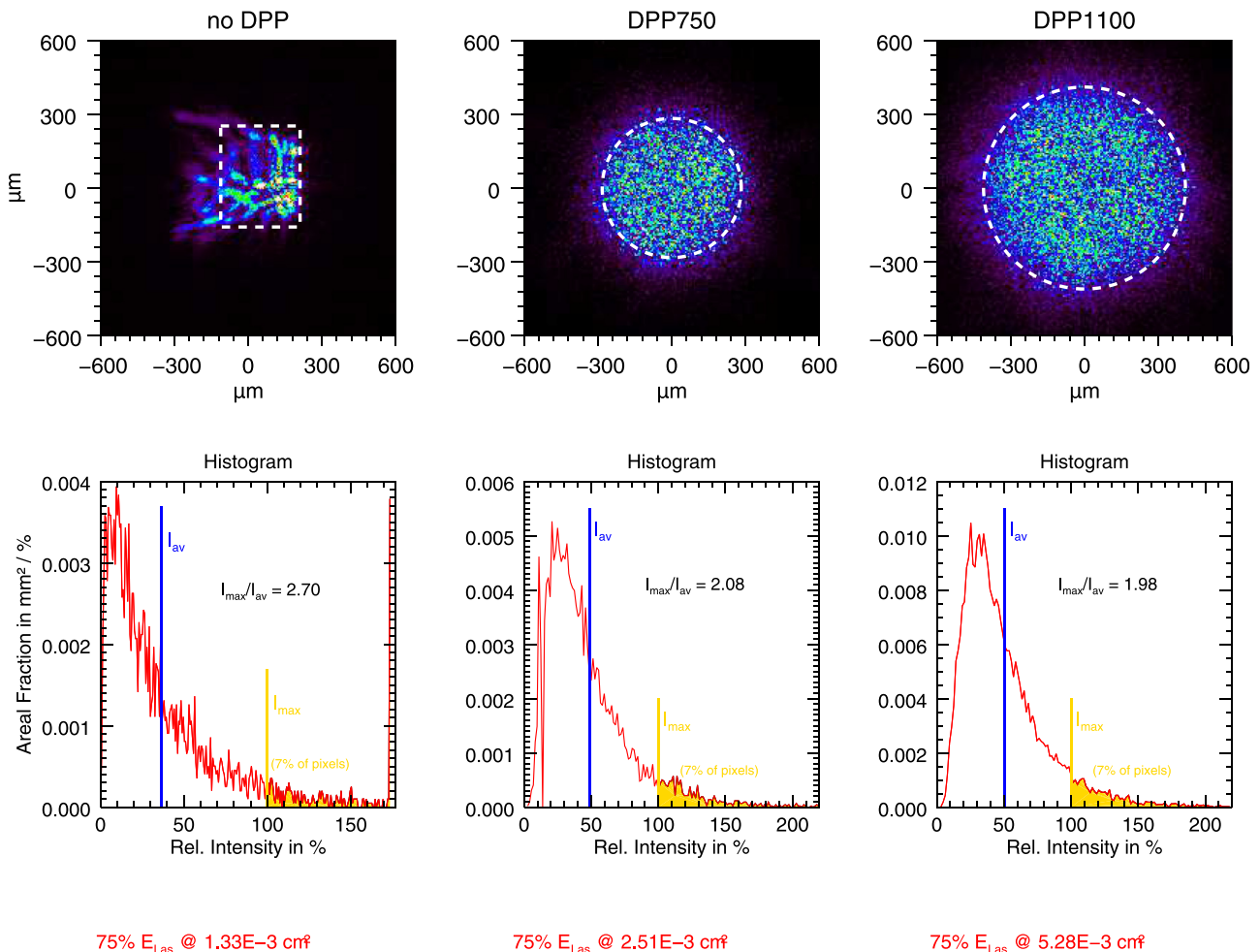


FIG. 6. Focus images for the unconditioned beam and the two distributed phase plates as recorded in the PECOS target chamber. The shape and size of the areas containing 75% of the laser energy are given by white dashed lines and red annotations.

We find that HYDRA significantly exaggerates the axial propagation depth of the laser for 100 TW/cm² or higher, while agreement with experiments (see Sec. VI, Fig. 14) is best with the lower intensity case. Figure 7 shows snapshots of the 50 TW/cm² and 35 TW/cm² intensity simulations at times when the coupled energy into the gas is comparable. The 35 TW/cm² case is shown at the end of the laser pulse while the more intense case is shown at 1.75 ns, nearly 2 ns before the end of the laser pulse. Laser absorption continues in the gas but the agreement with experiment is already poor. Note that the lower intensity case shows a wider radial distribution of deposited energy. The 100 TW/cm² case is not included but burns through the gas even faster.

From these results, it is clear that simply reducing SBS is not equivalent to better modeling of the configuration. The 20 J of SBS measured, for the 50 TW/cm² case, is insignificant compared to the total laser energy, perhaps indicating that the reflected energy is negligible (assuming similarly low SRS). From the standpoint of HYDRA simulations, this amounts to well over 500 J more available to couple, as compared to the lowest intensity case, and so contributes to the extended propagation. Since the propagation length in the experiments was very similar, this indicates additional important processes. While SRS is not measured in the experiments, estimates can be obtained (as described above) through NEWLIP post-processing of the HYDRA simulations.

Figure 8 displays the calculated SBS and SRS spectra for the 50 TW/cm² and 35 TW/cm² cases. The color scale represents the gain averaged along the rays for each wavelength, at each time in the simulation. Gains exceeding 20 are considered noticeable and detrimental. Both the SBS and SRS gains are very low for the lower intensity case which is consistent with the negligible SBS measured in the experiment, as well as the better agreement with the simulated propagation depth.

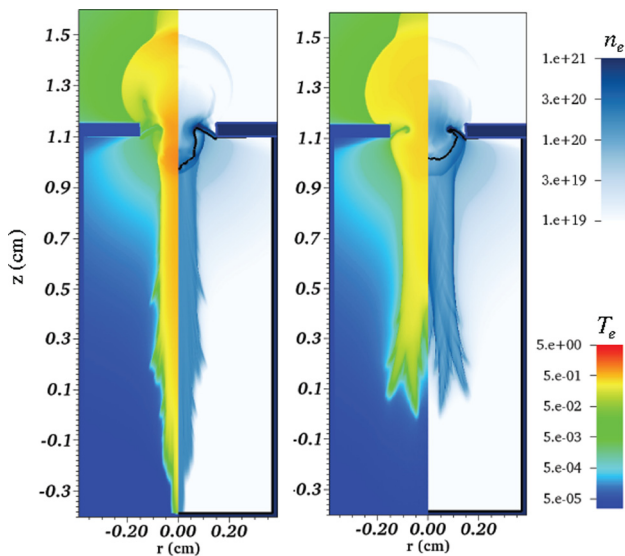


FIG. 7. Electron density and temperature for HYDRA simulations of experiments with 50 TW/cm² (left) and 35 TW/cm² (right) at times where the coupled energy to the gas is comparable. The case of higher intensity shows significantly deeper propagation at a faster rate. Experiments eventually falsified this increase, most likely as a result of increased LPI. The lower intensity case shows bend filaments near the end of the propagation. Such features can lead to an observable bifurcation of the laser deposition.

The 50 TW/cm² case shows a large increase in both SBS and SRS gains. SRS and SBS show bursts occurring almost immediately after the main pulse turns on and continues for over 1 ns. Culprits for these bursts are laser interaction with the ablated plastic window as well as self-intensification on axis much deeper into the gas. Such self-focusing is a manifestation of filamentation and is clearly observed in the HYDRA simulations, particularly near the axis. This effect increases the intensity and can lead to substantial SRS and SBS gain, as just described. This is likely contributing to shorter observed propagation depths at high intensities as compared to HYDRA predictions. NEWLIP predicts a significant blue-shift of the total spectrum, which is not observed experimentally as portrayed in Fig. 4. A possible explanation could be the overestimation of hydra for deposited energy in the gas, as well as difficulties with accurately modeling the LEH interaction and the transition from a solid window to the plasma state.

Though these results are generally qualitative, the large gain exponents for the 50 TW/cm² case are indicative of significant LPI and likely reflection of power. Reflected energy early in the laser pulse could certainly reduce the propagation length observed in the simulation. These calculations motivate the need to include SRS diagnostics as well as temporal SBS diagnostics in Pecos in order to test the fidelity of NEWLIP estimations. The effects of filamentation, both thermal and pondermotive, are likely important but are also difficult to diagnose.

V. LEH TRANSMISSION RESULTS

As mentioned above, measurements of LEH window surrogates in vacuum can only give a lower boundary of the expected absorption with gas fill. However, it is safe to say that poor performing LEH/laser pulse scenarios will lead to poor performance in an integrated experiment. A number of experiments without pre-pulse were performed, and no transmission above the calorimeter's response threshold of approximately 20 J was recorded, nor did the camera pick up any signal on the forward scatter plate (we assume a similar threshold). Consequently, no detailed analysis will be presented. We assume that the pre-pulse is sacrificial, preparing the plasma for the main pulse interaction. A comparison of relative transmission measurements into the through-focus calorimeter for a variety of polymer window materials (Parylene-N, polyester/Mylar, and polyimide/Kapton) in dependence of thickness is shown in Fig. 9. One can observe that thinner windows transmit better with an almost linear trend and the influence of the material is minimal. The omission of a phase plate dramatically reduces the measured transmission.

A parametric scan of the influence of pre-pulse energies with respect to LEH transmission and backscatter was performed for three different classes of laser pulse shapes: 2 ns main pulse width (FWHM) at 0.7–1.0 TW, 2 ns main pulse width at 0.3–0.5 TW, and 3.5 ns main pulse width at 0.3–0.5 TW. Figure 10 shows the transmission recorded by a calorimeter behind the LEH in dependence of the pre-pulse energy. The calorimeter was covering an area with twice the width and height of the laser's cross section. As mentioned above, measurements without a pre-pulse did not register any energy on

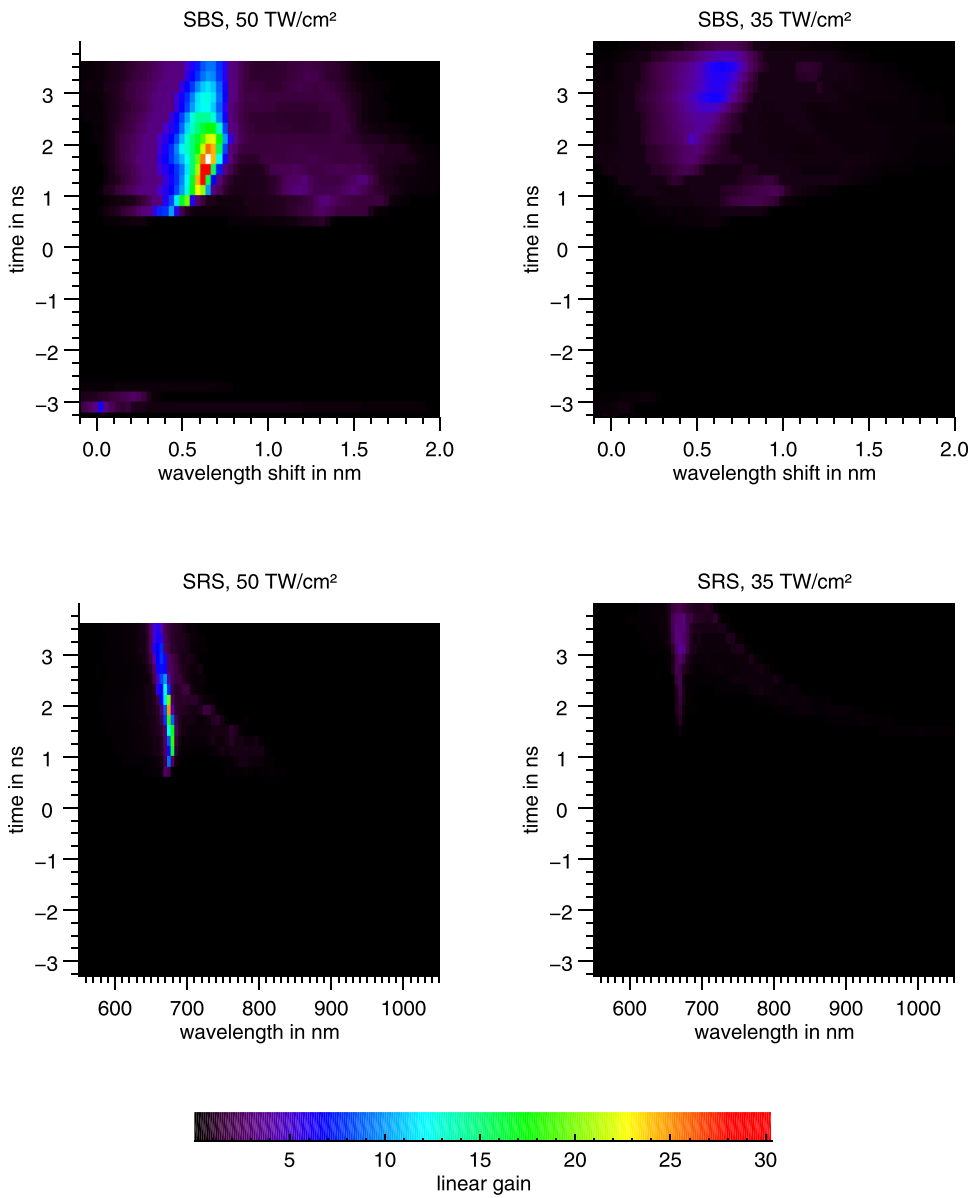


FIG. 8. NEWLIP results for the SBS (above) and SRS (below) calculations of linear gain with a 1100 μm DPP and 3.5 ns main pulse length. The left column represents experiments with 1200 J in the main pulse (50TW/cm²), and the right column with 850 J (35 TW/cm²).

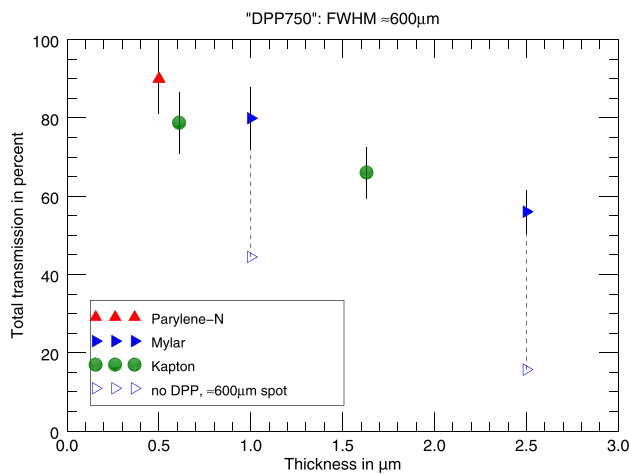


FIG. 9. Relative laser transmission versus thickness of the LEH window. The shots without phase plate were defocused to a spot area of approximately 600 μm , which is close to the FWHM diameter of Z-Beamlet's DPP750 phase plate.

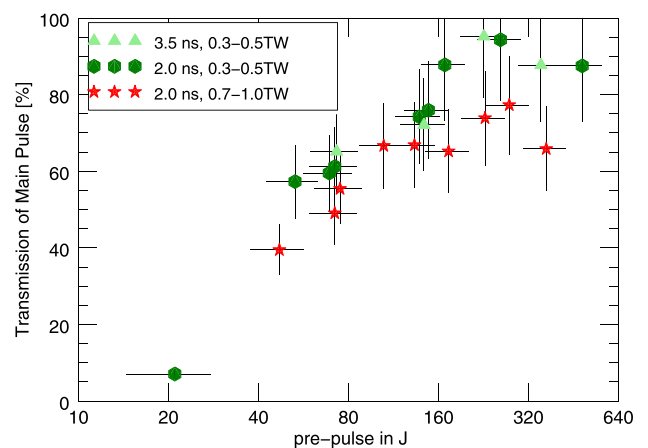


FIG. 10. Relative main pulse transmission versus pre-pulse energy for different main pulse widths and powers. All data were recorded using a 750 μm DPP and 1.47 μm thick polyimide LEH-windows.

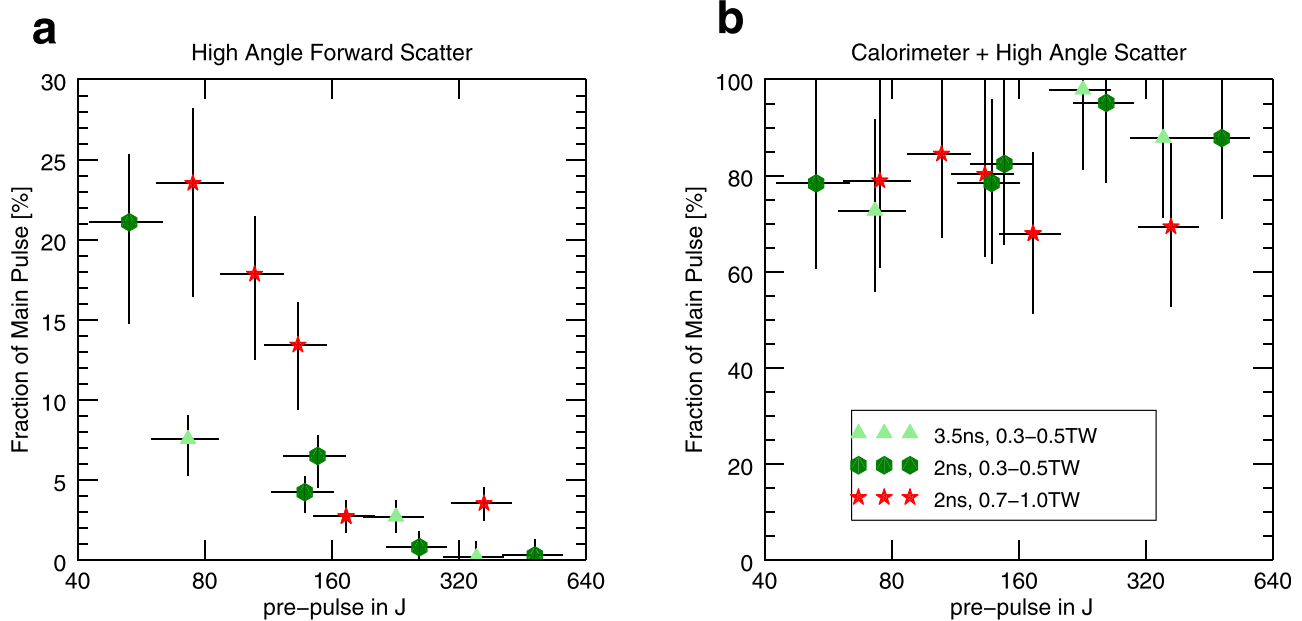


FIG. 11. Transmitted energy outside the calorimeter's aperture (a: angles larger than $F/5$) and total transmitted energy (b: scatter and calorimeter) for three different groups of main pulse powers and lengths. All experiments were performed with $1.47 \mu\text{m}$ polyimide windows and a DPP750.

the forward scatter plate or on the calorimeter. Consequently, all transmission measurements were scaled with respect to the main pulse while the pre-pulse is considered sacrificial. It is obvious that the registered transmission decreases for too low pre-pulse energies. Once the pre-pulse stays above approximately 160 J, there is no significant gain from increasing pulse energy. It can also be observed that the transmission consistently degrades for high laser power, while the length and energy content of the main pulse show no significant effect. All experiments used a distributed phase plate with a design diameter of $750 \mu\text{m}$ for 95% of encircled laser energy (DPP750) in the focal plane.

While the calorimeter registers less transmitted energy with decreasing pre-pulse [see Fig. 11(a)], there is more energy scattered into larger angles (outside of an $F/5$ aperture) with smaller pre-pulses. The LEH window expands less with smaller pre-pulses, and the resulting higher density can lead to stronger scatter effects, including both classical and nonlinear.

Furthermore, filamentation in the denser plasma can lead to features below the diffraction limit, allowing transmission angles that are higher than those included for the original F-number of the focusing optics. Figure 11 shows the energy of scattered light outside of the calorimeter's acceptance (a) and the sum of high-angle scatter and calorimeter transmission (b). Apparently, low pre-pulses cause so much high angle scatter that it makes up for the majority of the perceived transmission losses in the calorimeter. This observation is particularly pronounced for high main pulse powers. In fact, the total transmitted energy with inclusion of scattered light is nearly constant. The average transmission is still slightly higher for lower main pulse powers, but the difference is less pronounced than what the calorimeter measurements alone had implied. There is a possible lowering of total transmission for high main pulse powers and strong pre-pulses, and an increase for low main pulse powers and high pre-pulse levels, but the effect is subtle

compared to the measurement uncertainties. SBS backscatter is also increased for low pre-pulses, albeit at a lower level. Low main pulse powers seem to produce less SBS than high powers, and pre-pulses of at least 50 J seem to minimize SBS. There is no indication of an additional benefit for stronger pre-pulses than 50 J. Figure 12 shows the SBS measurements for all three previously considered main pulse groups.

The pre-pulse is mostly absorbed which is supported by relatively low observed backscatter and by a strong X-ray response of the LEH window during the interaction with the pre-pulse. All but a few shots show a very strong X-ray response with a modest response of the main pulse, while the rare cases of a pre-pulse below 50 J lead to a much stronger main pulse response. In the limits of the measurement precision, the X-ray signal of typical shots is proportional to the pulse energy of the incoming laser, accounting for a different conversion efficiency for the main and pre-pulse. However,

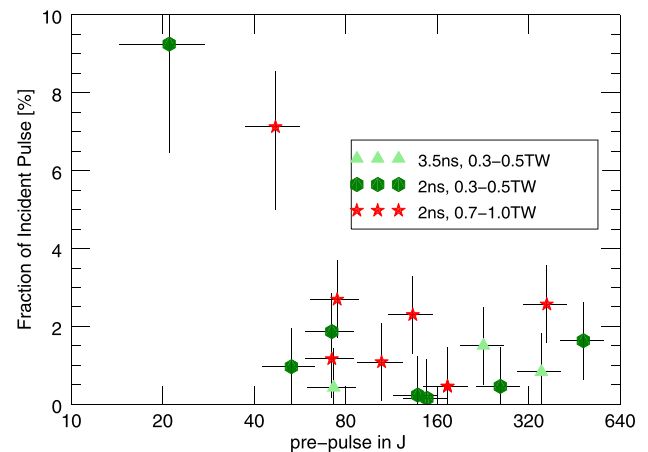


FIG. 12. SBS backscatter measurements from $1.47 \mu\text{m}$ polyimide windows for the three different groups of main pulse lengths and powers using a DPP750.

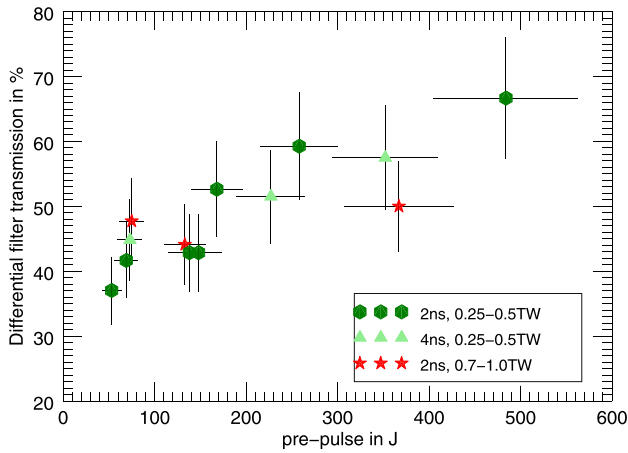


FIG. 13. Differential transmission of the main pulse's X-ray response through $6\ \mu\text{m}$ polyester measured by the ratio of two X-ray diodes (XRD1 without polyester, XRD2 with polyester filter).

the relative signal increase for the main pulse was different for the two differently filtered X-ray diodes. The changed signal ratio is a result of a change in the X-ray spectrum. Since there are no spectral lines for helium in the hard X-ray regime, the spectrum is defined by the black-body distribution of the plasma emission. Hence, the plasma temperature determines the filter's attenuation factor.

As shown in Fig. 13, one can see how the relative transmission through the additional $6\ \mu\text{m}$ polyester foil in XRD2 increases with pre-pulse energy implying increasing plasma temperatures. The LEH plasma is more effectively heated by the main pulse when being pre-shaped by a stronger pre-pulse, even though the laser transmission through the LEH plasma stays constant or even improves. Even in the vacuum transmission case, the comparatively short pre-pulse separation of 3.5 ns does not suffice to disperse the LEH plasma sufficiently. Instead, a strong pre-pulse produces a certain plasma scale length that increases the heating efficiency. A similar effect has previously been observed for the development of Sandia's X-ray backlighting capability, where 2–3 ns dwell times and 100–300 J pre-pulses increased the efficiency for helium-like Mn line radiation.³⁸ The stronger pulse also reduces the overall line density enough to balance absorption and reduce scatter efficiency since higher temperature plasmas have smaller scatter cross-sections. A conclusion is that the pre-pulse should be separated by a longer span as soon as the previously mentioned laser upgrade is completed, and longer dwell times between pre- and main pulse are obtainable. This should be even more important for integrated experiments in which the LEH window cannot expand as fast because it is backed by a high pressure deuterium fill.

VI. GAS CELL RESULTS

Not all combinations of LEH window and laser pulse shape that provide good transmission in vacuum are suited to heat deuterium fuel in a gas cell. The propagation of the main laser pulse in the fuel is impacted by the conditions of the frontal plasma that the pre-pulse has set up, many of which are

not characterized by LEH transmission studies. Furthermore, as mentioned above, the LEH window will decompress much more slowly when backed by several atmospheres of gas, particularly if this gas is heated to temperatures of tens or hundreds of eV. In an ideal case, the laser would “drill” into the fuel along a narrow channel that is widened to a slight down-tapered cone since the frontal plasma has more time to expand and absorbs more energy than the plasma at the end of the deposition range. Filamentation and scatter effects can distort this shape, and thus LPI effects can potentially be observed in a shadowgraph of the heated fuel region. Shadowgraphy and SBS near-beam-imaging were used to investigate the influence of a variety of laser pulse shapes interacting with a fuel cell. Confirming that SBS should fall exponentially with intensity, a dramatic reduction of SBS could be observed by introducing a variety of measures to lower the intensity in the focus compared to the slightly defocused 1 TW-laser pulse that had been used so far for the most successful integrated MagLIF experiments.⁶ It must be noted that the current MagLIF platform does not yet employ a phase plate to condition the focus intensity. Figure 14 shows the progress for laser heating by implementing a phase plate that is roughly equivalent in footprint to the defocused laser (step 1), reducing power by stretching the main laser pulse from 2 ns to 3.5 ns (step 2), swapping the phase plate from a $750\ \mu\text{m}$ design diameter to a $1100\ \mu\text{m}$ design diameter (step 3), and finally reducing the main pulse energy by approximately a factor of two (step 4). While the observed reduction of SBS is striking, it can also be observed that the conical component of the heated fuel's shadow becomes less pronounced with reduced intensity, as is the “bulbous feature” or “wing” in the first part of the propagation, both of which are not observed in simulations (see Fig. 7). The bifurcation of the laser deposition region in the last shadowgraph may very well be correlated to filamentation such as predicted in the HYDRA simulations shown in Fig. 7. Figure 14 also contains the SBS data for stand-alone LEH window transmission measurements in parentheses. While these measurements cannot exactly reproduce the case for a gas cell with 54 psi helium, it is likely that the value of LEH contributions is similar, since the density in a more slowly decompressing window would go up while the scale length stays shorter. Under this assumption, one finds that the SBS for high main pulse intensities is dominated from interaction in the gas, while the LEH window dominates the SBS contributions for intensities below $100\ \text{TW}/\text{cm}^2$. The latter is a result of the relatively high electron density in the LEH plasma. Even a fairly high pre-pulse of just over 300 J by itself ($250\ \text{TW}/\text{cm}^2$, the blue data point in Fig. 15) produces only a few Joules of SBS, which shows that most of the recorded SBS must be caused by the main pulse (note that even though the graph in Fig. 15 shows the SBS conversion for the pre-pulse at a similar level as many full pulse train experiments, the absolute amount is less since the pre-pulse contains much less energy than a full pulse train). Another observation is that high intensities tend to enhance transverse flares or jets, which are not yet fully understood. These features may have a potential to compromise the target's performance by heating the upper (frontal) peripheral regions of the target boundaries and thus shifting energy deposition from pre-heat to mix. It is

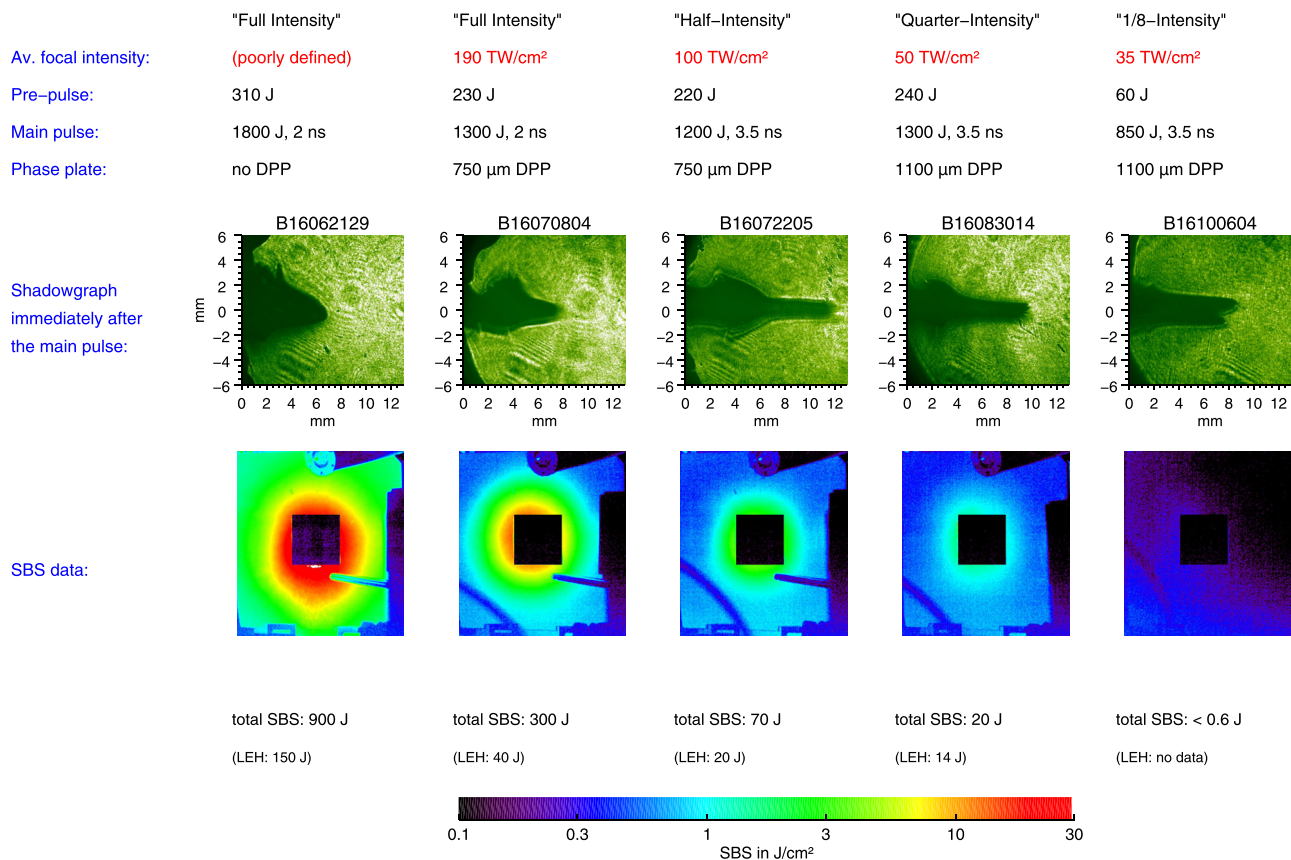


FIG. 14. Four-step improvement of laser pre-heat by reducing the laser intensity as described in the text.

difficult to properly characterize these distortions, but SBS is a very quantifiable measurement of degrading laser plasma interaction. Figure 15 shows the summary of all SBS measurements with gas cells. The data set includes shots without phase plate, with the DPP750, and the DPP1100. The pulse length of the main pulse was either 2 ns or 3.5 ns. Only on a logarithmic scale can the reduction of SBS by intensity reduction be properly displayed. The figure contains indications of SBS thresholds for 1 mm and 5 mm plasma length as guidance for upper and lower relevant thresholds. Even below the 1 mm threshold, a pulse can create significant early SBS if it is above the filamentation threshold (purple) because the intensity can be increased above the initial value. The measurements indicate that the original integrated MagLIF experiments with unconditioned foci were far above LPI thresholds and even after the introduction of a phase plate, LPI was still significant. Only by reducing beam power and ultimately enlarging the focus size could a reduction by more than two orders of magnitude be achieved. Considering that intensities were supposedly above the thresholds for SBS in a 5 mm plasma and for filamentation, measured SBS values in the order of 1% for intensities of 50–80 TW/cm² appear to be lower than expected. In comparison, measurements by Fernández *et al.*²¹ recorded 10% SBS or more by exceeding the threshold by a similar factor. It is possible that the used formulas, which were dominantly developed for different plasma parameters, do not translate perfectly to MagLIF relevant plasmas.

The X-ray diode measurements for gas cells experiments are shown in Fig. 16. Similar to the LEH transmission

experiments, one finds that (within measurement uncertainties) the X-ray response steadily increases with the laser pulse's energy as shown in Fig. 16(a). However, the main pulse causes a much stronger response compared to the experiments with stand-alone LEH windows as one can see for a diode trace in Fig. 16(b). This is a result of the combined effects of higher LEH window density due to slower decompression and an additional response from helium. The window's response decays as the laser keeps heating it because both the density and stopping power of the heated plasma decay. The gas response decays mostly because of the 18° observation angle of the X-ray diode with respect to the laser beam's axis. The

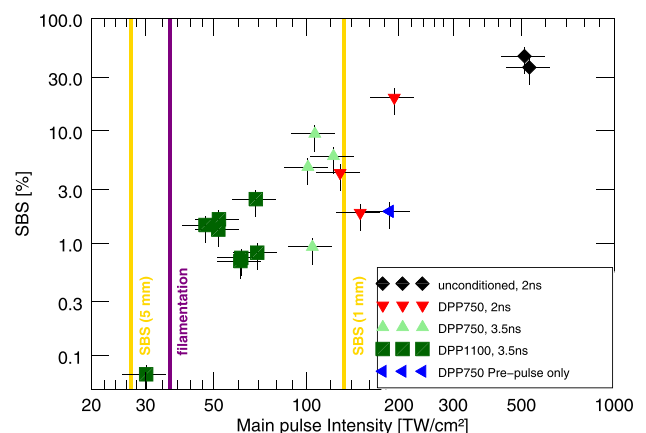


FIG. 15. Synopsis of SBS measurements for gas cells filled with 54 psi of helium for various focus conditioning measures and main pulse lengths. Solid colored lines indicate relevant LPI thresholds.

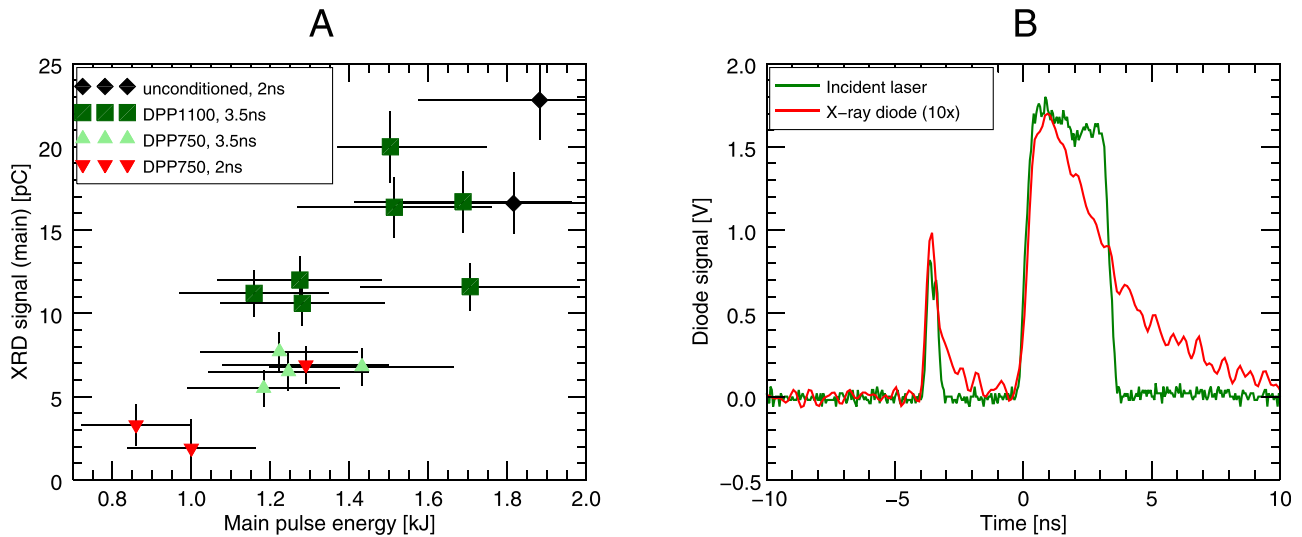


FIG. 16. X-ray diode data for gas cells with 54 psi helium fill and 1.7 μm thick polyimide LEH-windows.

hottest part of the plasma is near the end of the laser's range for each time step, continuously moving deeper into the target and out of vision through the LEH aperture. Neither the four steps that improved the laser heating with respect to SBS nor the shape of the heated plasma in the gas cell appears to influence the X-ray response of the target.

VII. SUMMARY

MagLIF experiments with the Z-Beamlet laser at a wavelength of 527 nm require the use of a pre-pulse for efficient pre-heat of the fuel. With modest intensities and the current pre-pulse separation time of 3.5 ns, the strength of the pre-pulse should be 160–200 J and can be reduced for main pulse intensities below 50 TW. SBS can be extremely important and reject up to 50% of the incident main pulse. In order to mitigate SBS and high angle forward scatter, and to optimize the shape of the heated plasma volume, the introduction of distributed phase plates was required but not sufficient. Stretching the main pulse in length and using a relatively large phase plate (DPP1100) proved sufficient to reduce SBS to the single-percent level. By additionally reducing the energy of the main pulse from 1800 J (no DPP, 2 ns main pulse) to 850 J (DPP1100, 3.5 ns main pulse), the absolute SBS level could be reduced by three orders of magnitude without an apparent loss of laser propagation depth. Most likely, the balance of the laser energy in the unconditioned case is partly backscattered and partly directed away from the target axis and posing a mix risk for integrated experiments. These two loss mechanisms seem to dominate over increased absorption in the window. SBS seems to be consistently reduced to 0.5%–3% as long as the average intensity of the main pulse is below 80 TW/cm². The current laser pre-heat conditions can be reached without generation of SBS, and additional beam conditioning techniques seem not yet relevant.

VIII. OUTLOOK

While the occurrence and mitigation of SBS has been characterized, and improved heating performance was observed

by lowering the main pulse intensity, the amount of SRS must yet be measured for MagLIF pre-heat experiments, particularly for gas cell experiments. This characterization along with a study of the benefit from prolonging the dwell time between pre- and main pulse will have high priority for subsequent campaigns at Z-Beamlet. The latter should provide a better understood pre-plasma since lower pre-pulse intensities and energies can be used leading to less LPI during the LEH-window disassembly. As last steps to complete surrogacy for the integrated experiments in Z, the Pecos target area is undergoing improvements to provide a B-field for fuel magnetization, and a flammable gas permit is pursued to perform experiments with deuterium instead of resorting to helium as a fuel surrogate.

2D HYDRA simulations show that even low SBS regimes can be difficult to model without the full picture of LPI. This is an additional motivation to diagnose SRS and filamentation processes as well as investigate techniques to mitigate high intensity interactions with the plastic window.

The insights gained by these experiments will help to improve integrated MagLIF experiments on Z. The increase of pre-heat energy for MagLIF is a multi-faceted effort of which backscatter suppression is only one aspect. It will likely be achieved by increasing the fuel density with careful control of LPI as shown in this study (larger phase plate, longer and lower main pulse) since this will ultimately be required to increase target gain towards the original paper's¹ point design values. Significantly increased densities may even require the implementation of frequency tripling, additional beam smoothing techniques such as SSD and polarization smoothing, or more novel and advanced concepts such as STUD pulses³⁹ for future MagLIF programs.

ACKNOWLEDGMENTS

The authors would like to acknowledge J. M. Koning and M. M. Marinak for HYDRA code support as well as D. J. Strozzi for NEWLIP support.

Sandia National Laboratories is a multi-mission laboratory managed and operated by National Technology and Engineering Solutions of Sandia, LLC., a wholly owned

subsidiary of Honeywell International, Inc., for the U.S. Department of Energy's National Nuclear Security Administration under Contract No. DE-NA0003525. This work has been supported by the "Accelerating Low-Cost Plasma Heating and Assembly" Program (ALPHA) of the Advanced Research Projects Agency-Energy (ARPA-E) within the U.S. Department of Energy.

- ¹S. A. Slutz, M. C. Herrmann, R. A. Vesey, A. B. Sefkow, D. B. Sinars, D. C. Rovang, K. J. Peterson, and M. E. Cuneo, *Phys. Plasmas* **17**, 056303 (2010).
- ²S. A. Slutz and R. A. Vesey, *Phys. Rev. Lett.* **108**, 025003 (2012).
- ³P. K. Rambo, I. C. Smith, J. L. Porter, M. J. Hurst, C. S. Speas, R. G. Adams, A. J. Garcia, E. Dawson, B. D. Thurston, C. Wakefield *et al.*, *Appl. Opt.* **44**(12), 2421 (2005).
- ⁴D. C. Rovang, D. C. Lamma, M. E. Cuneo, A. C. Owen, J. McKenney, D. W. Johnson, S. Radovic, R. J. Kaye, R. D. McBride, C. S. Alexander *et al.*, *Rev. Sci. Instrum.* **85**, 124701 (2014).
- ⁵A. B. Sefkow, S. A. Slutz, J. M. Koning, M. M. Marinak, K. J. Peterson, D. B. Sinars, and R. A. Vesey, *Phys. Plasmas* **21**, 072711 (2014).
- ⁶M. R. Gomez, S. A. Slutz, A. B. Sefkow, D. B. Sinars, K. D. Hahn, S. B. Hansen, E. C. Harding, P. F. Knapp, P. F. Schmit, C. A. Jennings *et al.*, *Phys. Rev. Lett.* **113**, 155003 (2014).
- ⁷C. Labaune, E. Fabre, A. Michard, and F. Briand, *Phys. Rev. A* **32**, 577 (1985).
- ⁸D. H. Froula, L. Divol, N. B. Meezan, S. Dixit, J. D. Moody, P. Neumayer, B. B. Pollock, J. S. Ross, and S. H. Glenzer, *Phys. Rev. Lett.* **98**, 085001 (2007).
- ⁹R. P. Drake, R. E. Turner, B. F. Lasinski, E. A. Williams, D. W. Phillion, K. G. Estabrook, W. L. Kruer, E. M. Campbell, K. R. Manes, J. S. Hildum, and T. W. Johnston, *Phys. Fluids* **31**(10), 3130 (1988).
- ¹⁰H. Figueroa, H. Joshi, H. Azechi, N. A. Ebrahim, and K. Estabrook, *Phys. Fluids* **27**(7), 1887 (1984).
- ¹¹D. B. Sinars, G. R. Bennett, D. F. Wenger, M. E. Cuneo, D. L. Hanson, J. L. Porter, R. G. Adams, P. K. Rambo, D. C. Rovang, and I. C. Smith, *Rev. Sci. Instrum.* **75**(10), 3672 (2004).
- ¹²G. R. Bennett, M. C. Herrmann, M. J. Edwards, B. K. Spears, C. A. Back, E. W. Breden, P. J. Christenson, M. E. Cuneo, K. L. Dannenberg, C. Frederick *et al.*, *Phys. Rev. Lett.* **99**, 205003 (2007).
- ¹³R. D. McBride, S. A. Slutz, C. A. Jennings, D. B. Sinars, M. E. Cuneo, M. C. Herrmann, R. W. Lemke, M. R. Martin, R. A. Vesey, K. J. Peterson *et al.*, *Phys. Rev. Lett.* **109**, 135004 (2012).
- ¹⁴Y. Kato, K. Mima, N. Miyanaga, S. Arinaga, M. Nakatsuka, and C. Yamanaka, *Phys. Rev. Lett.* **53**, 1057 (1984).
- ¹⁵S. N. Dixit, J. K. Lawson, K. R. Manes, H. T. Powell, and K. A. Nugent, *Opt. Lett.* **19**(6), 417 (1994).
- ¹⁶Y. Lin, T. J. Kessler, and G. N. Lawrence, *Opt. Lett.* **20**(7), 764 (1995).
- ¹⁷S. Skupsky, R. W. Short, T. Kessler, R. S. Craxton, S. Letzring, and J. M. Soures, *J. Appl. Phys.* **66**(8), 3456 (1989).
- ¹⁸K. Tsubakimoto, M. Nakatsuka, H. Nakano, T. Kanabe, T. Jitsuno, and S. Nakai, *Opt. Commun.* **91**, 9 (1992).
- ¹⁹R. H. Lehberg, A. J. Schmitt, and S. E. Bodner, *J. Appl. Phys.* **62**, 2680 (1987).
- ²⁰B. J. MacGowan, B. B. Afeyan, C. A. Back, R. L. Berger, C. Bonnaud, M. Casanova, B. I. Cohen, D. E. Desenne, D. F. DuBois, A. G. Dulieu *et al.*, *Phys. Plasmas* **3**, 2029 (1996).
- ²¹J. C. Fernández, B. S. Bauer, J. A. Cobble, D. F. DuBois, G. A. Kyrala, D. S. Montgomery, H. A. Rose, H. X. Vu, R. G. Watt, B. H. Wilde *et al.*, *Phys. Plasmas* **4**, 1849 (1997).
- ²²C. Niemann, L. Divol, D. H. Froula, G. Gregori, O. Jones, R. K. Kirkwood, A. J. MacKinnon, N. B. Meezan, J. D. Moody, C. Sorce *et al.*, *Phys. Rev. Lett.* **94**, 085005 (2005).
- ²³S. H. Glenzer, D. H. Froula, L. Divol, M. Dorr, R. L. Berger, S. Dixit, B. A. Hammel, C. Haynam, J. A. Hittinger, J. P. Holder *et al.*, *Nat. Phys.* **3**, 716 (2007).
- ²⁴S. Atzeni and J. Meyer-ter-Vehn, *The Physics of Inertial Fusion* (Oxford University Press, 2004).
- ²⁵D. S. Montgomery, *Phys. Plasmas* **23**, 055601 (2016).
- ²⁶R. L. Berger, C. H. Still, E. A. Williams, and A. B. Langdon, *Phys. Plasmas* **5**, 4337 (1998).
- ²⁷S. Hüller, P. Mounaix, and D. Pesme, *Phys. Scr. T* **63**, 151 (1996).
- ²⁸B. I. Cohen, H. A. Baldis, R. L. Berger, K. G. Estabrook, E. A. Williams, and C. Labaune, *Phys. Plasmas* **8**, 571 (2001).
- ²⁹P. Neumayer, R. L. Berger, L. Divol, D. H. Froula, R. A. London, B. J. MacGowan, N. B. Meezan, J. S. Ross, C. Sorce, L. J. Sluter, and S. H. Glenzer, *Phys. Rev. Lett.* **100**, 105001 (2008).
- ³⁰R. K. Kirkwood, B. J. MacGowan, D. S. Montgomery, B. B. Afeyan, W. L. Kruer, J. D. Moody, K. G. Estabrook, C. A. Back, S. H. Glenzer, M. A. Blain *et al.*, *Phys. Rev. Lett.* **77**(13), 2706 (1996).
- ³¹C. H. Still, R. L. Berger, A. B. Langdon, D. E. Hinkel, L. J. Suter, and E. A. Williams, *Phys. Plasmas* **7**, 2023 (2000).
- ³²A. J. Schmitt and B. B. Afeyan, *Phys. Plasmas* **5**, 503 (1998).
- ³³J. Myatt, A. V. Maximov, W. Seka, R. S. Craxton, and R. W. Short, *Phys. Plasmas* **11**, 3394 (2004).
- ³⁴D. H. Froula, L. Divol, and S. H. Glenzer, *Phys. Rev. Lett.* **88**(10), 105003 (2002).
- ³⁵S. H. Glenzer, L. J. Suter, R. E. Turner, B. J. MacGowan, K. G. Estabrook, M. A. Blain, S. N. Dixit, B. A. Hammel, R. L. Kauffman, R. K. Kirkwood *et al.*, *Phys. Rev. Lett.* **80**(13), 2845 (1998).
- ³⁶M. M. Marinak, R. E. Tipton, O. L. Landen, T. J. Murphy, P. Amendt, S. W. Haan, S. P. Hatchett, C. J. Keane, R. McEachern, and R. Wallace, *Phys. Plasmas* **3**, 2070 (1996).
- ³⁷D. J. Strozzi, E. A. Williams, D. E. Hinkel, D. H. Froula, R. A. London, and D. A. Callahan, *Phys. Plasmas* **15**, 102703 (2008).
- ³⁸D. B. Sinars, G. R. Bennett, M. C. Herrmann, I. C. Smith, C. S. Speas, L. E. Ruggles, and J. L. Porter, *Rev. Sci. Instrum.* **77**, 10E306 (2006).
- ³⁹B. J. Albright, L. Yin, and B. Afeyan, *Phys. Rev. Lett.* **113**, 045002 (2014).